LA-UR-18-28529
Approved for public release; distribution is unlimited.

Title: High Dose Ion Irradiation Testing on Improved HT-9 Alloys

Author(s): Aydogan, Eda
Chancey, Matthew Ryan
Wang, Yongqiang
Clausen, Bjorn

Intended for: Report

Issued: 2018-09-06

Disclaimer:
Los Alamos National Laboratory, an affirmative action/equal opportunity employer, is operated by the Los Alamos National Security, LLC for the National Nuclear Security Administration of the U.S. Department of Energy under contract DE-AC52-06NA25396. By approving this article, the publisher recognizes that the U.S. Government retains nonexclusive, royalty-free license to publish or reproduce the published form of this contribution, or to allow others to do so, for U.S. Government purposes. Los Alamos National Laboratory requests that the publisher identify this article as work performed under the auspices of the U.S. Department of Energy. Los Alamos National Laboratory strongly supports academic freedom and a researcher's right to publish; as an institution, however, the Laboratory does not endorse the viewpoint of a publication or guarantee its technical correctness.

High Dose Ion Irradiation Testing on Improved HT-9 Alloys

Fuel Cycle Research & Development

Prepared for
U.S. Department of Energy
Advanced Fuels Campaign

Eda Aydogan
Matthew Chancey
Yongqiang Wang
Bjorn Clausen

7/27/18

DISCLAIMER

Los Alamos National Laboratory, an affirmative action/equal opportunity employer, is operated by the Los Alamos National Security, LLC for the National Nuclear Security Administration of the U.S. Department of Energy under contract DE-AC52-06NA25396. By approving this article, the publisher recognizes that the U.S. Government retains nonexclusive, royalty-free license to publish or reproduce the published form of this contribution, or to allow others to do so, for U.S. Government purposes. Los Alamos National Laboratory requests that the publisher identify this article as work performed under the auspices of the U.S. Department of Energy. Los Alamos National Laboratory strongly supports academic freedom and a researcher's right to publish; as an institution, however, the Laboratory does not endorse the viewpoint of a publication or guarantee its technical correctness.

SUMMARY

HT9 alloys having various nitrogen contents were deformed up to 50% engineering strain by plane strain compression. Dislocation density and characteristics were determined after neutron diffraction using line profile analysis. These samples having low and high nitrogen contents were irradiated at 300 °C up to 23 peak dpa. In this study, effect of plane strain deformation on the radiation response of low and high N HT9 alloys has been investigated using both transmission electron microscopy and nanoindentation. It has been found that compression results in a considerable increase in both dislocation density and edge type dislocations. Both TEM and nano-indentation studies indicate that plane strain deformation results in improved radiation resistance in high N HT9 alloys. It has been also found that further deformation beyond 10% compression does not improve the radiation resistance further. On the other hand, deformation does not have a clear effect on the radiation resistance in the case of low N HT9 alloys. Together with that, ion irradiations at 300 °C results in ~2 times higher hardening in low N alloys compared to high N alloys.

TABLE OF CONTENTS

SUMMARY iv

1. Introduction 1

2. Materials and Methods 1

3. Results and Discussion 3

4. Conclusions and Future Work 10

5. References 10

Intentionally Blank

1. Introduction

Next generation advanced reactors are expected to operate at extreme conditions such as high temperatures and neutron damage levela as well as corrosive environments. HT-9 ferritic/martensitic steels are one of the best candidates for structural materials in nuclear applications such as first wall and blanket for fusion reactors, and the fuel cladding and fuel ducts for fast reactors [1]. Radiation induced swelling and hardening in candidate materials is a serious problem and therefore considerable effort has been spent to understand and reduce swelling and hardening under irradiation. There is a general perception that cold working or an increase in the dislocation density suppresses the radiation induced swelling [204,205]. However, it has been found that cold work might either reduce [2] or increase swelling [3], besides having no effect on it [4]. In this study, we investigated the effect of plane strain deformation on the defect evolution and radiation hardening in HT9 F/M alloys having different nitrogen contents.

2. Materials and Methods

HT9 alloys were produced with different nitrogen contents as shown in Table 1. Alloys were austenitized at 1040 °C for 30 min and air cooled followed by tempering at 760 °C for 1 h and air cooling. Samples were cut into cylindrical shape (5 mm in diameter and 8 mm in height) by electrical discharge machining (EDM). Then, the cylinders were compressed to 10%, 30% and 50% of engineering strain at room temperature. In order to determine the bulk dislocation density and their characteristics, neutron diffraction experiments have been performed at LANSCE. Line profile analyses have been conducted on the diffraction patterns to determine dislocation densities and types [5].

Table 1. Chemical composition of HT9 alloys in wt. %

Alloy ID	C	N	Cr	Mo	Si	Mn	Ni	V	W	Fe
HT9 Low N	0.20	0.001	11.07	1.0	0.25	0.55	0.51	0.30	0.47	Bal.
HT9 High N	0.20	0.044	11.42	1.0	0.26	0.56	0.52	0.30	0.48	Bal.

For ion irradiations, samples were EDMed in 3-mm disks from the deformed cylinders, mechanically ground, and polished with a final step of 0.04 µm colloidal silica. Mechanically polished disks were electropolished at 20 V using 10% percholoric acid-90% methanol solution at -40 °C. Heavy ion irradiations were performed using the NEC 3 MV Pelletron Tandem Ion Accelerator in the Ion Beam Materials Laboratory (IBML) at Los Alamos National Lab (LANL) using 5 MeV Fe^{2+} ions at 300 °C. The dose rate was ~$6x10^{-3}$ dpa/s. The complete series of doses included peak dpa of 1, 4, 8, 15 and 23. Figure 1 shows the SRIM calculated damage profiles with respect to depth for peak damages of all these irradiation conditions. Our analysis is focused in the depth range of 150-1000 nm where the damage is more uniform. The damage levels in this region are approximately 0.4, 1.8, 3.5, 6.6, 10.1 local dpa. The dose profiles were calculated using "Quick Calculation of Damage" option in SRIM with a displacement energy of 40 eV. The damage calculated with this option is based on the Kinchin-Pease formalism used in the NRT model [6]. This option is currently recommended for comparison with neutron damage [7]. Temperature was recorded using a K-type thermocouple in contact with the sample surface (not exposed to irradiation) to be 300±10 ºC. Target chamber vacuum was kept at ~$5x10^{-8}$ torr during irradiation. More details of the ion irradiation setup can be found elsewhere [8].

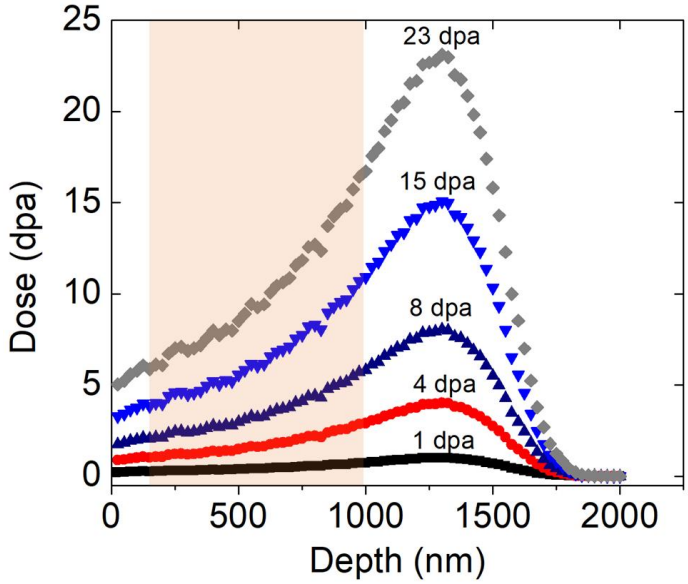

Figure 1. SRIM calculated damage profiles for 1, 4 and 16 local dpa with 5 MeV Fe ions using the displacement energy of 40 eV. The dashed red box indicates the region TEM analysis was performed in. Shaded region between 150 nm and 1000 nm is investigated.

Transmission electron microscopy (TEM) and detailed quantitative analysis were conducted on 6.6 dpa irradiation conditions for low N HT9 alloys. After irradiation, samples were prepared using conventional lift-out technique with a FEI Helios Dual Beam microscope. Lift-out cutting and thinning was performed at 30 kV and 16 kV followed by cleaning at 5 kV and 2 kV. An FEI Tecnai F30 TEM operating at 300 kV was used for dislocation loop investigation. Samples were tilted to g<110> kinematic condition from [111] zone axis. Bright field imaging and diffraction patterns were taken to calibrate the microscope rotations. Bright field scanning TEM (STEM) studies were conducted and correlated with the bright TEM images and diffractions. Types of the dislocations were determined from their shapes as reported by Yao et al. [9]. Moreover, electron energy loss spectroscopy (EELS) was performed to determine the thickness of the foils based on number of mean free paths, a well-known technique described in the literature [10]. Statistics on loop size and number density were obtained from at least 5 different regions.

Nanoindentation tests were performed on a Keysight G200 Nanoindenter with a diamond, pyramidal (Berkovich) tip to a final displacement of 1000 nm, a constant strain rate (loading rate divided by the load) of 0.05 s^{-1}, and with a continuous stiffness measurement (CSM) of 45 Hz frequency and 2 nm displacement amplitude. Hardness and modulus measurements were determined using the Oliver-Pharr method [11]. The tip contact area function was determined from tests on a fused silica standard with an indenter Young's modulus and Poisson's ratio of 1130 GPa and 0.07, respectively (diamond). A sample Poisson's ratio of 0.3 was used in the calculation of Young's modulus for HT9 samples. Arrays of indents were placed to cover multiple grains for each irradiation condition. The average hardness was determined over a displacement range of 150-250 nm. The plastic zone size, the depth of material probed, under the tip is approximately 4-10 times the indenter displacement [12]. In the irradiated material, it is closer to a factor of four times the indenter displacement based on experiments by Hardie et al. [12]. Thus an indentation depth of 150-250 nm corresponds to probing material as deep as 150-1000 nm which is well within the ion irradiated material at the surface. The commonly observed indentation size effect [13-16], higher hardness at shallower depths, was also considered in understanding the hardness trends with damage. The Nix-Gao model [13] was used to estimate the hardness at an infinite depth, H_o, and a length scale term, h^*, from hardness, H, and displacement, h, data between 150-250 nm according to Eqn. (1).

$$\frac{H}{H_o} = \sqrt{1 - \frac{h^*}{h}} \tag{1}$$

3. Results and Discussion

3.1. Microstructure and mechanical properties before irradiation

Figure 2 shows the microstructures of low and high N HT9 alloys before deformation. EBSD gray scale maps indicate that the lath structure is coarser in the case of high N HT9 compared to the low N alloy (Figure 2a). Moreover, BFTEM and STEM micrographs in Figure 2b show that there are large $M_{23}C_6$ carbides mostly along the lath boundaries in both alloys. On the other hand, needle-like vanadium carbo-nitrides exist within laths in the case of high N alloy as pointed by red arrows in the inset of high N micrograph in Figure 2b.

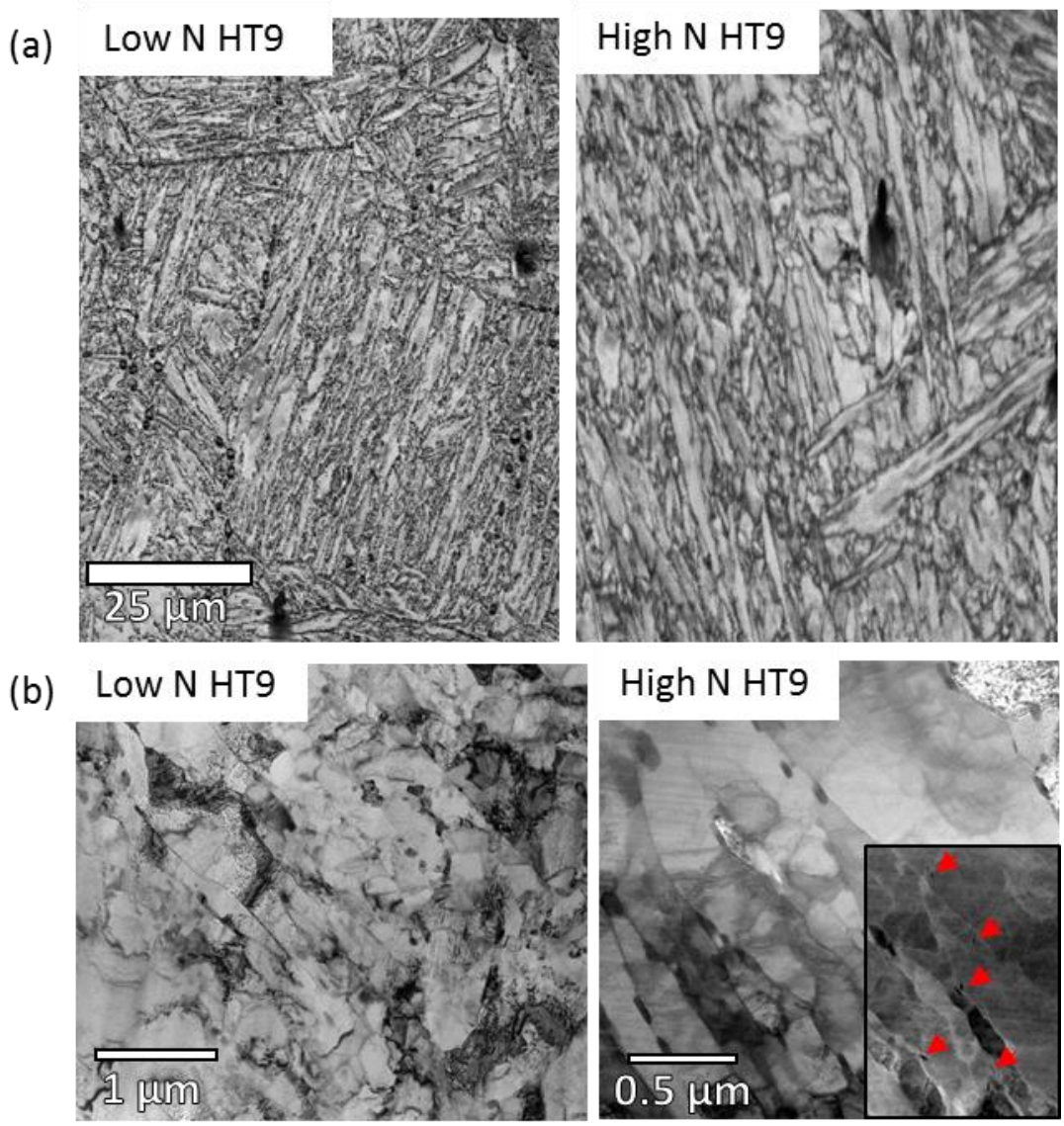

Figure 2. (a) EBSD gray scale maps and (b) BFTEM/STEM images of low and high N HT9 alloys. Red arrows in (b) indicate the V-C-N particles.

Figure 3 shows dislocation density, characteristics and Vickers hardness of the low and high N HT9 alloys with respect to the deformation amount. With increasing deformation up to 30%, while both low and high N HT9 alloys show increasing dislocation density, dislocation density in the case of high N HT9 alloys either decreased slightly or remained constant while dislocation density continues to increase with further

deformation, as shown in Figure 3a. Similarly, while the hardness either saturates or slightly increase after 30% deformation, it continues to increase in the case of low N HT9 alloys after 30% deformation (Figure 3b). By looking at both the dislocation and hardness profiles, it is reasonable to assume that both hardness and dislocation density saturate after 30% deformation; whereas, they continue increasing even after 50% deformation in the case of low N HT9 alloys. Figure 3c shows that the fraction of edge dislocations in both low and high N HT9 alloys is very low in undeformed condition. However, after 10% of compression, the portion of edge dislocations increases to ~60-70% and remains similar with further deformation.

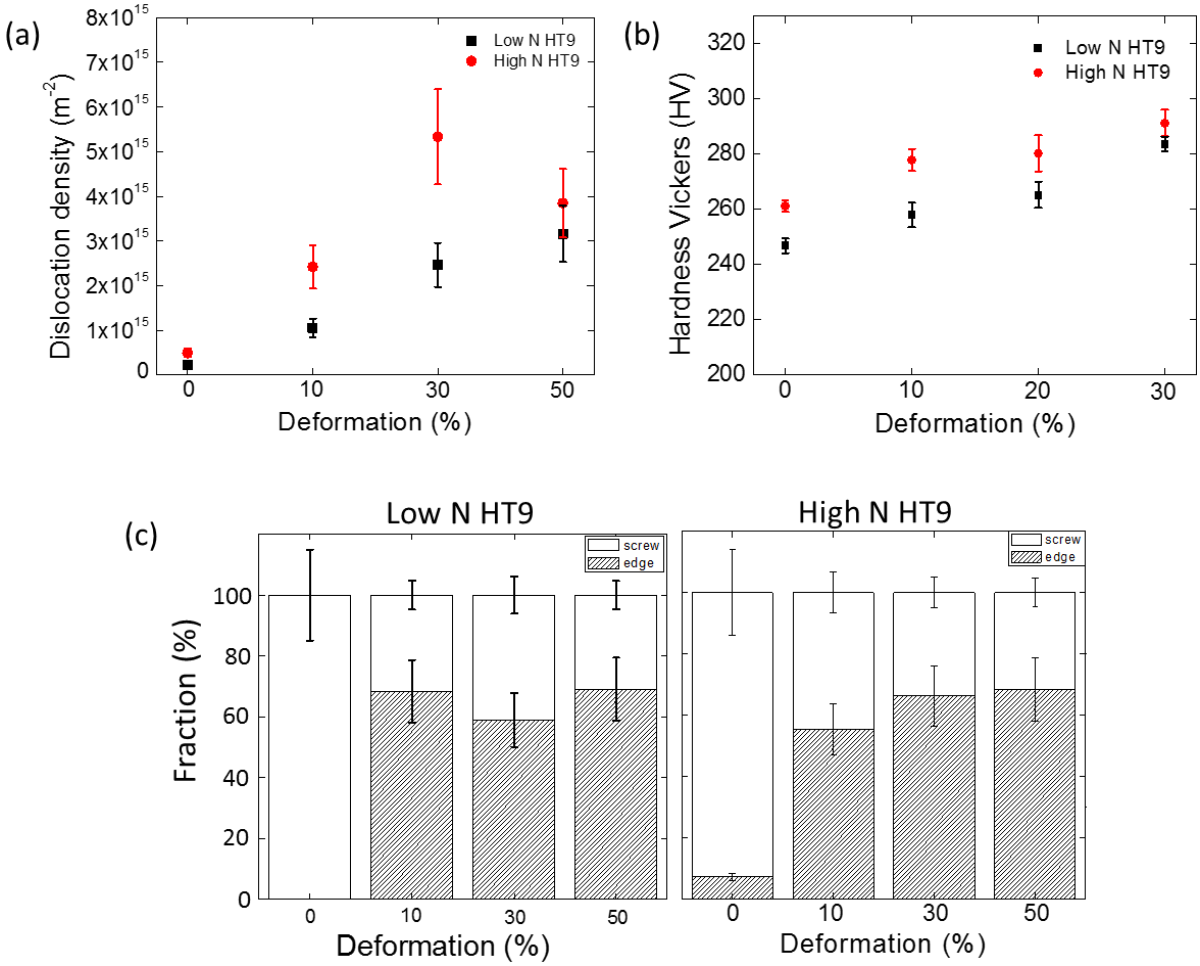

Figure 3. (a) Dislocation density vs. deformation amount plots for low and high N HT9 alloys obtained from neutron diffraction experiments, (b) Vickers hardness vs. deformation amount for low and high N HT9 alloys, (c) Fraction of screw and edge dislocations with respect to deformation in low and high N GT9 alloys.

3.2. Microstructure after irradiation

Detailed microstructural investigations have been conducted on ~6.6 dpa irradiated high N HT alloys. Samples were tilted from [111] zone axis and images were taken at g<110>. The loop sizes and densities were determined from the images taken at least 3 different locations in a grain. Moreover, error is represented by standard deviation in the measurements. Types of the dislocation loops can be determined from their shapes as seen in Figure 4. Red loops having large aspect ratio are <111> type loops while blue loops having aspect ratio close to 1 are <100> type loops. It should be noted that deformation results in

large dislocation network densities, both seen in micrographs and determined from the neutron diffraction experiments. Dislocation loops have been found to be either <100> or <111> type loops in this study.

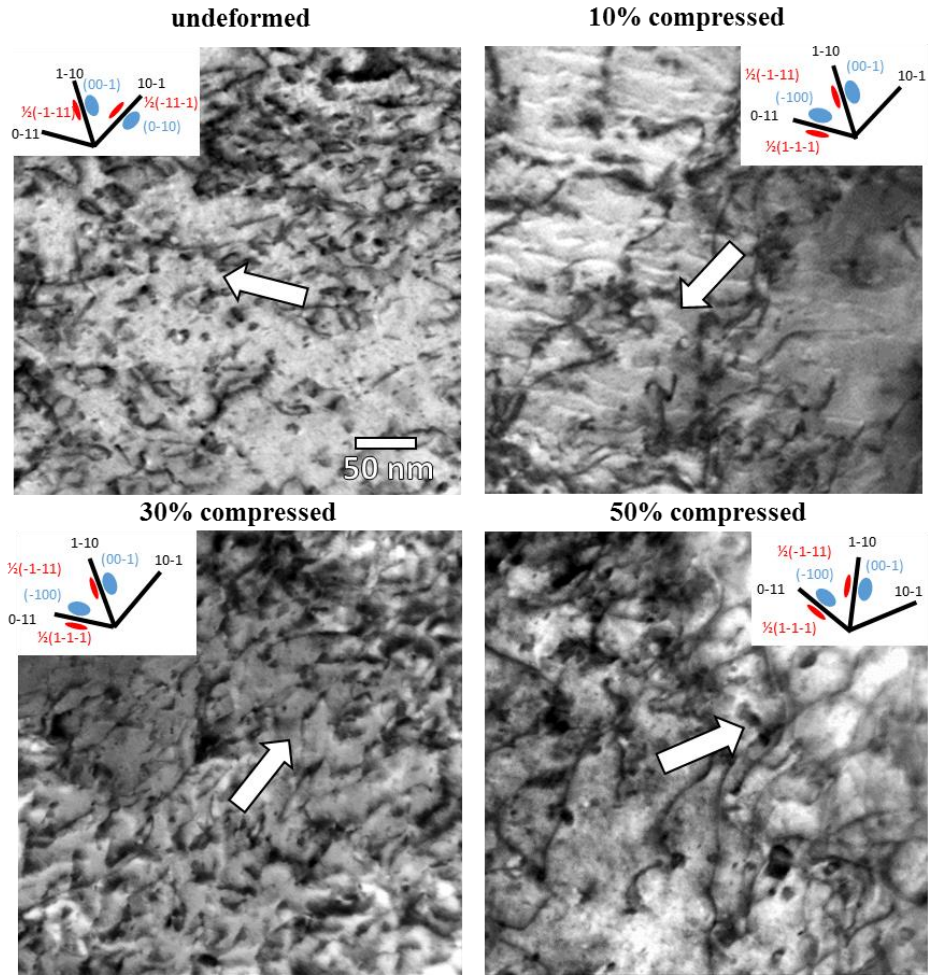

Figure 4. BF-STEM micrographs showing the dislocation loops after ~6.6. dpa at 300 °C in various deformation conditions. Arrow indicates the direction of g-vector.

Figure 5 shows the size distribution of the dislocation loops. Except for the case of 30% compression, loop size distribution becomes broader with increasing deformation. Moreover, especially 50% compressed sample shows a bimodal size distribution. Overall, the size of <100> loops is slightly smaller than that of <111> loops for all cases. Size of the <111> and <100> loops were determined to be 14.3±6.1 nm and 11.4±5.2 nm, respectively in undeformed HT9 alloy. In the case of 10% deformed alloy, size of the <111> and <100> loops were determined to be 18.2±6.8 nm and 14.4±6.3 nm, respectively. Moreover, <111> loop size is determined to be 13.7±4.4 nm and <100> loop size is determined to be 13.1±6.2 nm in 30% compressed sample while they are determined as 20.4±8.2 nm and 15.0±9.2 nm, respectively in the case of 50% compressed alloy. It should be noted that both loop sizes show skewness towards larger sizes in all cases. From the invisibility criteria, it is known that 1/2 of the <111> loops and 2/3 of the <100> loops can be seen along g<110> kinematic condition. In undeformed HT9 alloy, the number densities of <100> and <111> type loops have been calculated as $8.1\pm0.9\times10^{21}$ m^{-3} and $8.9\pm1.0\times10^{21}$ m^{-3}, respectively. Moreover, number densities of <100> loops have been calculated as $2.6\pm0.7\times10^{21}$ m^{-3}, $8.0\pm1.5\times10^{21}$ m^{-3} and $1.9\pm0.5\times10^{21}$ m^{-3} while number densities of <111> loops have been calculated as $2.0\pm0.6\times10^{21}$ m^{-3}, $7.0\pm1.2\times10^{21}$ m^{-3} and $1.8\pm0.9\times10^{21}$ m^{-3} for 10%, 30% and 50% compressed samples respectively.

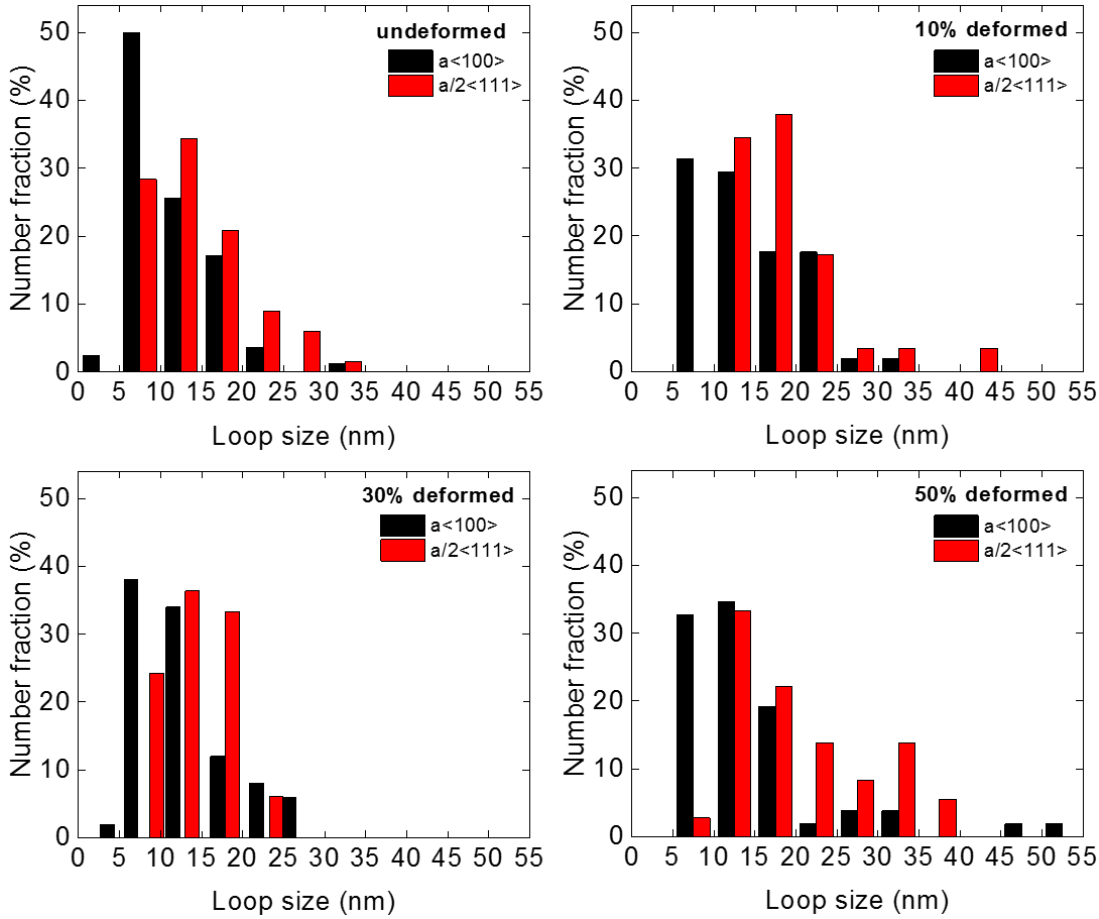

Figure 5. Dislocation loop types and their size distribution in undeformed, 10%, 30% and 50% compressed samples after ~6.6. dpa at 300 °C.

Figure 6 shows the dislocation loop size and density with respect to deformation amount. Size of the loops in undeformed and 30% deformed conditions are smaller compared to the ones in 10% and 50% deformed HT9 alloys, as shown in Figure 6a. On the other hand, number density of loops in undeformed and 30% deformed samples is much larger compared to the ones in 10% and 50% deformed samples (Figure 6b). It should also be noted that the fraction of <100> and <111> loops are almost the same for all conditions. If the damage (per nm) is defined as total loop area/total volume, it can be found that maximum damage occurs in the case of undeformed sample, as shown in Figure 6c. As expected from the loop size and density measurements, 30% deformed sample shows second higher damage formation while 10% and 50% deformed samples show the lowest damage formation after ~6.6 dpa irradiation at 300 °C. This infers that plane strain compression improves the radiation resistance of high N HT9 alloys. 30% deformed sample shows higher damage compared to the other deformed samples, which might be attributed to the error in the TEM analysis and poor statistics.

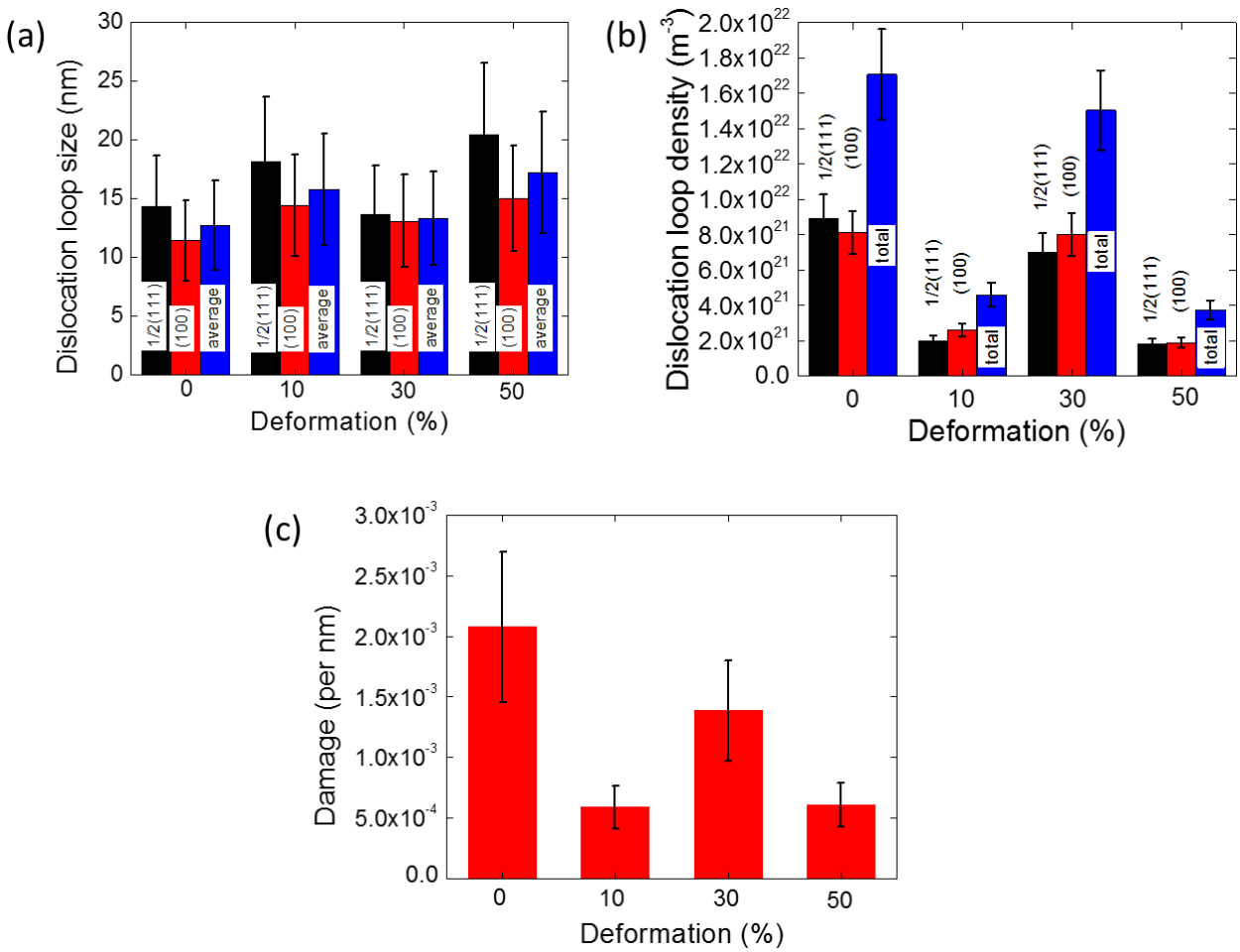

Figure 6. (a) Loop sizes of <111> and <100> loops together with their overall average vs. deformation amount plot; (b) Loop densities of <111> and <100> loops together with their total vs. deformation plot; (b) damage (total loop area/total volume) with respect to the deformation amount in the HT9 alloys.

Figure 7 shows a STEM image of undeformed high N HT-9 sample from an irradiated region where the peak dpa was ~15. Elemental mapping on this region indicated that there are different types of particles in the microstructure. Elongated and circular large particles are determined to be Cr-W-Mn-Si-Mo-C-N-S rich particles. These are M23X6 particles which are present before irradiation. Moreover, there are V-C-N rich particles which are also present in the unirradiated condition. However, Ni map indicates the formation of fine particles after irradiation. These particles are most probably G-phase which is rich in Ni, Si and W.

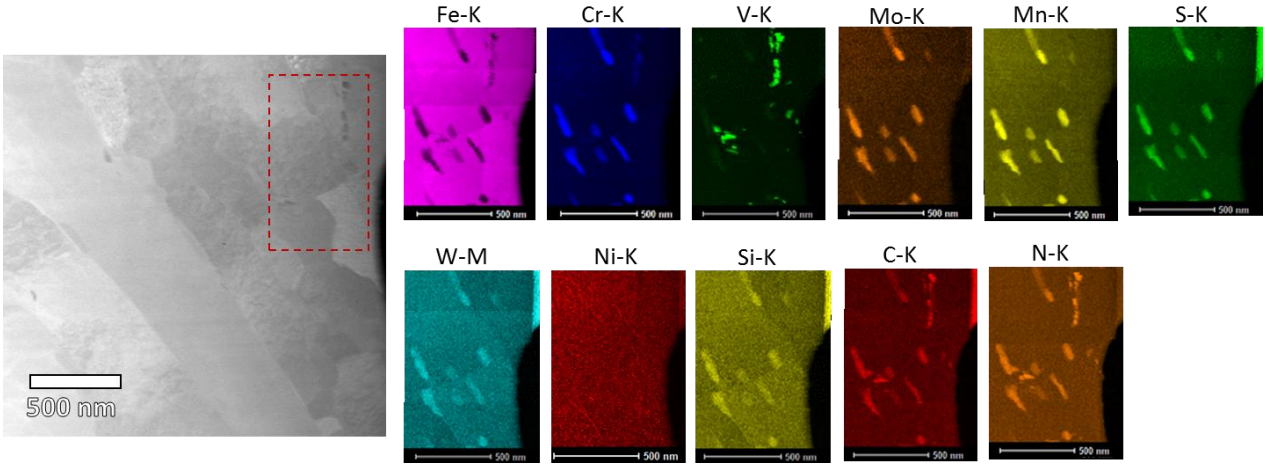

Figure 7. Elemental mapping within the irradiation range in undeformed high N HT9 alloy irradiated to ~6.6 dpa at 300 °C. Red box on the STEM image corresponds to the EDX maps.

3.3. Mechanical properties after irradiation

Figure 8 shows the hardness vs. dose profiles for low and high N HT9 alloys in undeformed, 10%, 30% and 50% deformed conditions. It has been found that the hardness of both low and high N alloys is ~0.5 GPa lower in undeformed condition compared to the deformed conditions before irradiation. Moreover, the nanohardness of low N alloys is lower than that of high N alloys before irradiation, which agrees with the microhardness measurements. In the undeformed low N HT9 alloy, the hardness increases from ~3 GPa to ~5.5 GPa after irradiation up to ~10 dpa. In the case of deformed low N HT9 alloys, hardness increases from ~4 GPa to ~6 GPa. In all cases, hardness seems to be saturated after ~2 dpa. In the case of undeformed high N alloy, hardness increases from ~3.5 GPa to ~5 GPa after irradiation up to ~10 dpa. On the other hand, in deformed samples, hardness increases from ~4.5 GPa to ~5.5 GPa. Similar to the low N HT9 alloys, high N alloys show saturation in hardness after ~2 dpa of irradiation.

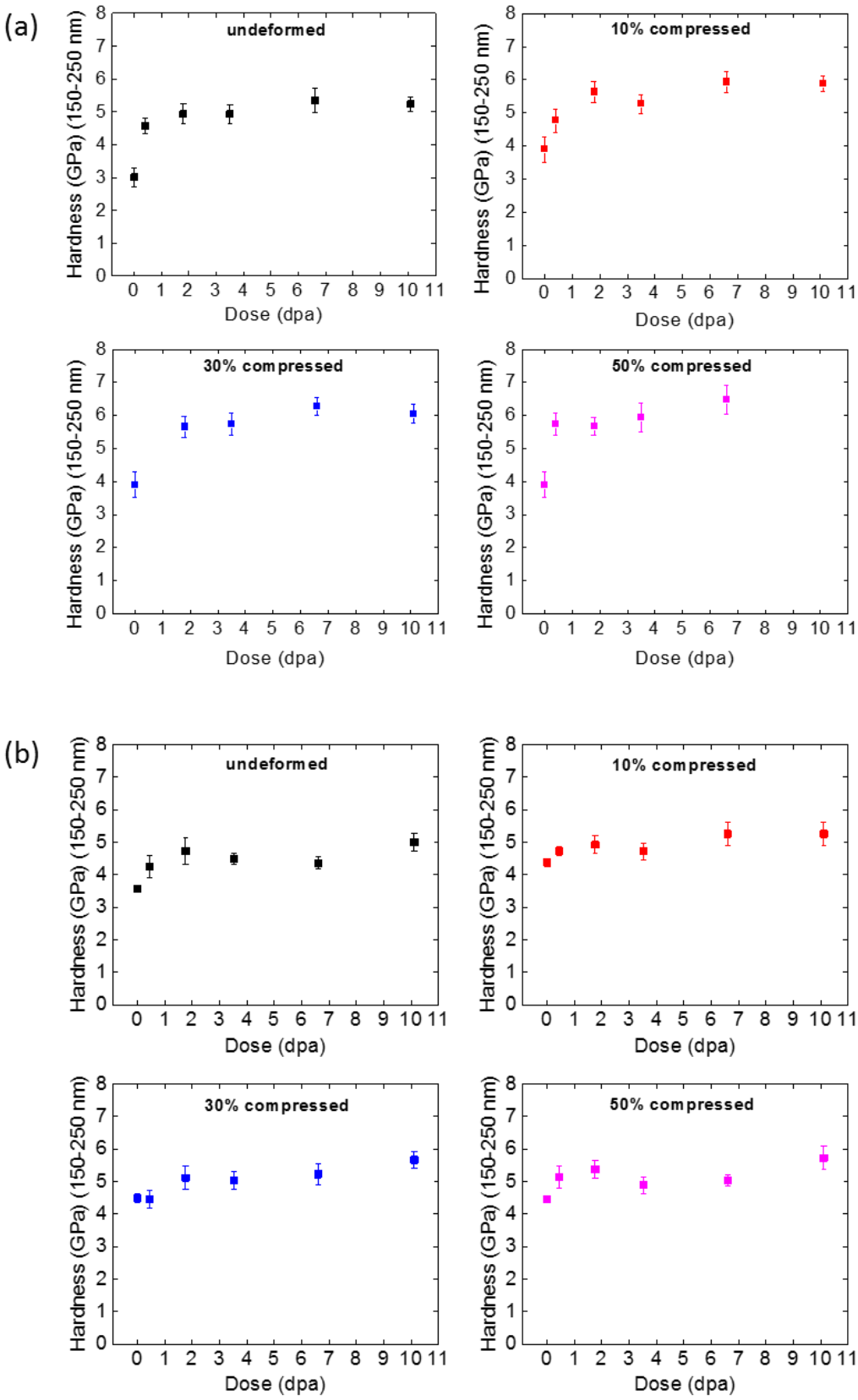

Figure 8. Hardness vs dose profiles for (a) low N HT9 alloys in undeformed, 10%, 30% and 50% deformed conditions; (b) high N HT9 alloys in undeformed, 10%, 30% and 50% deformed conditions.

Figure 9 summarizes the hardening due to ion irradiation at 300 °C with respect to deformation amount in both low and high N HT9 alloys. It is obvious that the hardening in low N HT9 alloys is higher compared to the high N alloys. Moreover, deformation does not improve the radiation hardening (damage as a result of irradiation) in the case of low N alloys. However, even though the hardening is within the error, deformation seems to decrease hardening, therefore improve the radiation resistance in high N HT9 alloys.

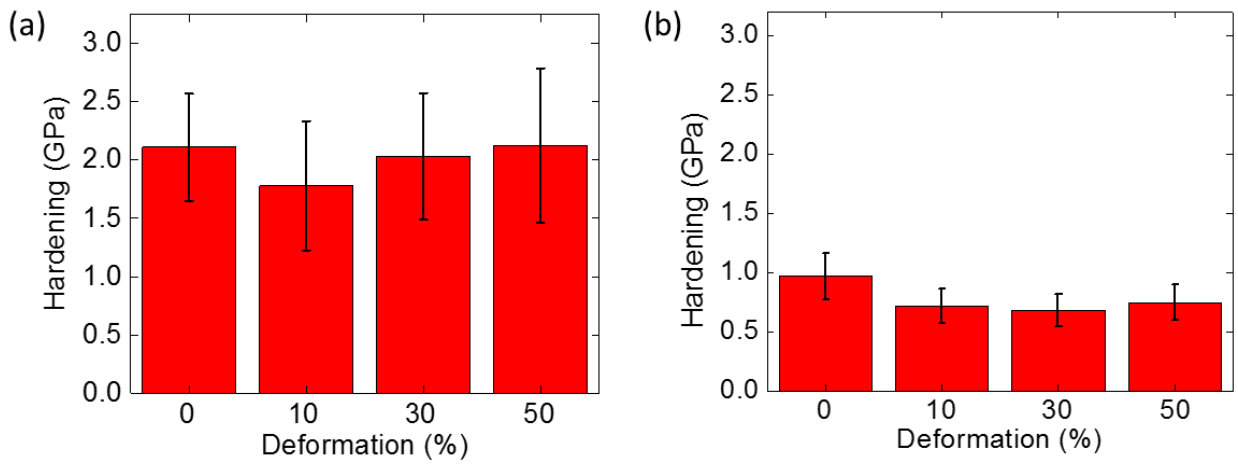

Figure 9. Hardening vs. deformation plots for (a) low N and (b) high N HT9 alloys.

4. Conclusions and Future Work

In this work, effect of plane strain deformation on the radiation response of low and high N HT9 alloys has been investigated using both transmission electron microscopy and nanoindentation. It has been found that compression results in a considerable increase in both dislocation density and edge type dislocations. Both TEM and nano-indentation studies indicate that plane strain deformation results in improved radiation resistance in high N HT9 alloys. It has been also found that further deformation beyond 10% compression does not improve the radiation resistance further. On the other hand, deformation does not have a clear effect on the radiation resistance in the case of low N HT9 alloys. Together with that, ion irradiations at 300 °C results in ~2 times higher hardening in low N alloys compared to high N alloys. In high N alloys, both <100> and <111> type loops formed after ~6.6 dpa irradiation. The fraction of these loops were found to be similar. TEM investigations on loop size and density are underway for low N HT9 alloys.

5. References

[1] R.L. Klueh, A.T. Nelson, Journal of Nuclear Materials, 371 (2007) 37-52.
[2] W. K. Appleby, E. E. Bloom, J. E. Flinn, F.A. Garner, Proceedings of International Conference on Radiation Effects in Breeder
Reactor Structural Materials, AIME, New York, (1977) 509-527.
[3] A. Risbet, V. Levy, J. Nucl. Mater., v. 46, no. 3, pp. 341-352.
[4] V. Levy, J. Mathie, A. Risbet, R. Levy , J.P. Poirier, Voids Formed by Irradiation of Reactor Materials, British Nuclear Society, Reading, United Kingdom, (1971) 63-69.
[5] L. Balogh, D.W. Brown, P. Mosbrucker, F. Long, M.R. Daymond, Acta Materialia, 60 (2012) 5567-5577.
[6] J.F. Ziegler, Nuclear Instruments and Methods in Physics Research Section B: Beam Interactions with Materials and Atoms, 219–220 (2004) 1027-1036.

[7] R.E. Stoller, M.B. Toloczko, G.S. Was, A.G. Certain, S. Dwaraknath, F.A. Garner, Nuclear Instruments and Methods in Physics Research Section B: Beam Interactions with Materials and Atoms, 310 (2013) 75-80.
[8] E. Aydogan, J.S. Weaver, S.A. Maloy, O. El-Atwani, Y.Q. Wang, N.A. Mara, Journal of Nuclear Materials, 503 (2018) 250-262.
[9] B. Yao, D.J. Edwards, R.J. Kurtz, Journal of Nuclear Materials, 434 (2013) 402-410.
[10] T. Malis, S.C. Cheng, R.F. Egerton, Journal of Electron Microscopy Technique, 8 (1988) 193-200.
[11] W.C. Oliver, G.M. Pharr, J Mater Res, 19 (2004) 3-20.
[12] C.D. Hardie, S.G. Roberts, A.J. Bushby, J Nucl Mater, 462 (2015) 391-401.
[13] W.D. Nix, H.J. Gao, Journal of the Mechanics and Physics of Solids, 46 (1998) 411-425.
[14] Y. Huang, F. Zhang, K.C. Hwang, W.D. Nix, G.M. Pharr, G. Feng, Journal of the Mechanics and Physics of Solids, 54 (2006) 1668-1686.
[15] J.G. Swadener, E.P. George, G.M. Pharr, Journal of the Mechanics and Physics of Solids, 50 (2002) 681-694.
[16] G.M. Pharr, J.H. Strader, W.C. Oliver, J Mater Res, 24 (2009) 653-666.